An ensemble neural network approach for space-time landslide predictive modelling

Jana Lim[a, b, *], Giorgio Santinelli[b], Ashok Dahal[a], Anton Vrieling[a], Luigi Lombardo[a]

[a] ITC, Faculty of Geo-Information Science and Earth Observation, University of Twente, The Netherlands
[b] Deltares, The Netherlands
*correspondence to: s.x.j.lim@utwente.nl

Abstract

There is an urgent need for accurate and effective Landslide Early Warning Systems (LEWS). Most LEWS are currently based on a single temporally-aggregated measure of rainfall derived from either *in-situ* measurements or satellite-based rainfall estimates. Relying on a summary metric of precipitation may not capture the complexity of the rainfall signal and its dynamics in space and time in triggering landslides. Here, we present a proof-of-concept for constructing a LEWS that is based on an integrated spatio-temporal modelling framework. Our proposed methodology builds upon a recent approach that uses a daily rainfall time series instead of the traditional cumulated scalar approximation. Specifically, we partition the study area into slope units and use a Gated Recurrent Unit (GRU) to process a satellite-derived rainfall time series and combine the output features with a second neural network (NN) tasked with capturing the effect of terrain characteristics. To assess if our approach enhances accuracy, we applied it in Vietnam and compared it against a standard modelling approach that incorporates terrain characteristics and cumulative rainfall over 14 days. Our protocol leads to better performance in hindcasting landslides when using past rainfall estimates (CHIRPS), as compared to the standard modelling approach. While not tested here, our approach can be extended to rainfall obtained from weather forecasts, potentially leading to actual landslide forecasts.

Keywords

Space-time modelling; deep learning; gated recurrent units; landslide early warning systems; Vietnam

1. Introduction

Future climate projections and environmental changes indicate growing landslide risks (IPCC, 2022), especially of rapid, rainfall-induced landslides (Gariano & Guzzetti, 2016). Hence, there is a growing urgency for reliable and accurate Landslide Early Warning Systems (LEWS). Such LEWS provide warnings to communities that are threatened by the hazard, thus allowing them to respond accordingly to reduce the possibility of harm to lives, properties, and infrastructure. LEWS fall into two categories: 1) physically-based and 2) data-driven methods (Pecoraro et al., 2019; Stanley et al., 2020). The former corresponds to a class of models that solve the governing

hydro-mechanical equations behind the initiation and evolution of landslides (Park et al., 2019). Such models are primarily constrained to site-scale applications due to the demanding data requirements related to geotechnical characteristics. Conversely, data-driven methods can be extended to regional and global scales using open-access datasets (Stanley et al., 2021). In both cases, the conventional basis of a LEWS involves establishing thresholds on rainfall characteristics that relate to the triggering of landslides (Segoni et al., 2018). For example, this can be achieved by establishing rainfall intensity-duration thresholds, above which, it is likely for a landslide to occur in a given area (Saito et al., 2010). As a result, warnings are issued when these rainfall thresholds are exceeded (Chleborad et al., 2006).

We see two areas for mprovement in predicting rainfall-induced landslides. Firstly, thresholds for forecasting rainfall-induced landslides have been derived exclusively on the basis of rainfall data without regard for terrain characteristics (Zêzere et al., 2015). Secondly, these thresholds are based on a single temporally-aggregated measure of precipitation (Segoni et al., 2015). Regarding the first point, the spatial and temporal dimensions of a landslide occurrence are typically treated separately although the likelihood of landslide occurrences are not independent of the combination of time and local environmental conditions. This assumed stationarity has been challenged due to altered spatio-temporal dynamics of rainfall characteristics resulting from climate change (Samia et al., 2017; Loche et al., 2022) and anthropogenic actions that disturb slope equilibria, for example land use modifications (Reichenbach et al., 2014; Hao et al., 2020). Quantifying susceptibility in both time and space is imperative in understanding the physical and dynamic processes associated with instability (Guzzetti et al., 1999; Stefanini, 2004). On the second point, the standard use of a single aggregate measure of cumulative rainfall (Segoni et al., 2015) neglects the granular information contained in a rainfall time series. A recent study by Fang et al. (2023) has established that using a time series of daily rainfall observations, as opposed to its representation as a single cumulative value, leads to better landslide predictions. In that study, a deep learning (DL) approach using recurrent neural networks (RNN) was implemented to predict occurrences and non-occurrences of landslides based on the rainfall signal.

The use of DL is not new to landslide prediction efforts, especially in the context of traditional susceptibility. For instance, convolutional neural networks are particularly suited for processing gridded data, and have therefore been applied widely in studies that use such data for mapping susceptibility (Wang et al., 2019; Fang et al., 2020). Beyond the context of gridded data, neural networks (NN) have also proven effective; for example triangular irregular networks were used for susceptibility models with a graph-based structure to carry the inherent spatial dependencies of covariates (Zeng et al., 2022). Architectures that can handle temporal variations of the response and predictor variables remain relatively unexplored in landslide studies, with the exception of predicting individual slope displacement (e.g. Nava et al., 2023). These applications primarily exploit variants of RNN (Mayoraz & Vulliet, 2002), such as Long Short Term Memory (Zhang et al., 2022) and Gated Recurrent Units (GRU) (Nava et al., 2023) to regress the time series of terrain displacement obtained from GPS (Ma et al., 2021) or InSAR (Chen et al., 2021) against rainfall time series. Such architectures have not been extensively applied to modelling spatio-temporal probabilities of landslide occurrences due to the scarcity of quality multi-temporal landslide inventories. As reported by Guzzetti et al. (2012), most existing landslide databases

were and still are geomorphological inventories that contain landslides mapped either as a point or a polygon without the time of occurrence. Besides geomorphological databases, there are also multi-temporal and event-based inventories. These are associated with temporal information on landslide occurrences. Multi-temporal inventories characterise a given territory over long time spans and can be obtained from magazines, damage reports, online sources, field surveys or remote mapping. Instead, event-based inventories comprise landslides that happen in response to a single trigger, resulting in more precise temporal information, at times as detailed as the day or hour of occurrence. The recent study by Mondini et al. (2023) showcases how detailed spatio-temporal landslide information fed to a DL architecture may be used as a basis for LEWS. Despite the architectural novelty, their contribution only uses the rainfall signal without incorporating terrain characteristics. This is the same for the model proposed by Fang et al. (2023). Moreover, Fang and co-authors also made use of a coarse, grid-based partitioning of the landscape, inevitably losing the link to slope instability processes.

Here, we extend the work by Fang et al. (2023) and Mondini et al. (2023) to a data-scarce context, still regressing the rainfall time series as a whole and combining that with terrain characteristics. Specifically, we make use of a subset of a multi-temporal inventory (Amatya et al., 2022) in Vietnam. We partition the study area into slope units (SUs), incorporate terrain characteristics that are typical of susceptibility models, and use GRUs to handle the entire precipitation signal.

Vietnam was intentionally selected as the study region because of the challenges associated with conducting susceptibility studies in data-poor contexts. By this, we mean that most of the data – either in the form of landslides, rainfall or terrain characteristics – could only be obtained through open-source and global repositories without the inclusion of local measurements. While several studies have focused on assessing the spatial landslide susceptibility in Vietnam (e.g. Bien et al., 2023; Le Minh et al., 2023; Ngyuen et al., 2023), few studies have attempted to link spatio-temporal patterns of the trigger to the landslide hazard (Ahmed et al., 2023; Moreno et al., 2023, Gian et al., 2017; Nhu et al., 2019). For example, Tien et al. (2013) introduced a 15-day cumulative rainfall threshold to develop spatial and temporal landslide probability maps, but besides rainfall no other environmental factor was used. This may have led to the erroneous high-alert warnings in flat areas. Furthermore, the rainfall data in that study was derived from rain gauge stations, which were not always near the landslide occurrence locations, thereby potentially poorly representing the rainfall characteristics. While the modelling framework employed by Ahmed et al. (2023) accounted for interactions between the spatial and temporal components of the landslide hazard, the study focused exclusively on the northern part of Vietnam. In addition, the framework was based on a Bayesian version of a binomial Generalized Additive Model informed by the rainfall pattern as a function of scalar cumulative rainfall. In other words, their study was a step towards a unified LEWS, albeit still based on a traditional use of cumulative rainfall data.

2. Study area

With its complex topography (elevation ranges from sea level to 3098m) and location in the tropical monsoon zone, rainfall-induced landslides regularly occur in Vietnam, particularly between May and October (Duc, 2013; Tien et al., 2017). Landslide occurrences are aggravated by anthropogenic modification processes, such as deforestation (Pham et al., 2021), mining and

slope cutting for road building (Nguyen et al., 2020). Northern provinces in particular, such as Lao Cai, Ha Giang, Yen Bai and Son La, are among the most frequently affected by landslides (Pham et al., 2020).

Our study regions are shown in Figure 1A-C, and were demarcated based on the footprints of the Planet imagery used to build the landslide inventory (Amateya et al., 2022). We constrained our analysis to areas in proximity of the mapping footprints to avoid assuming that no landslides occurred outside them. The study areas span across 10 provinces in Vietnam. These are mainly in the north, with two provinces in the centre and one in the south. Central Vietnam receives the highest amount of rainfall (Figure 1D), and peak rainfall occurs between May and October, when rainfall depth is about 12 times higher as in the dry season (Figure 1E). A number of active faults dissect the landscape within and in the vicinity of Vietnam, particularly in the North. These faults are responsible for weathered bands around the main tectonic lines (Thinh et al., 2016), thick mylonitic deposits (Lepvrier et al., 2011), and decreased rock mass strength (Duc et al., 2022). This may be the reason why a number of landslides have been reported in the northern sector of Vietnam (Hung et al., 2017; Van Tien et al., 2021), which is a signal that also appears in the inventory mapped by Amateya et al. (2022).

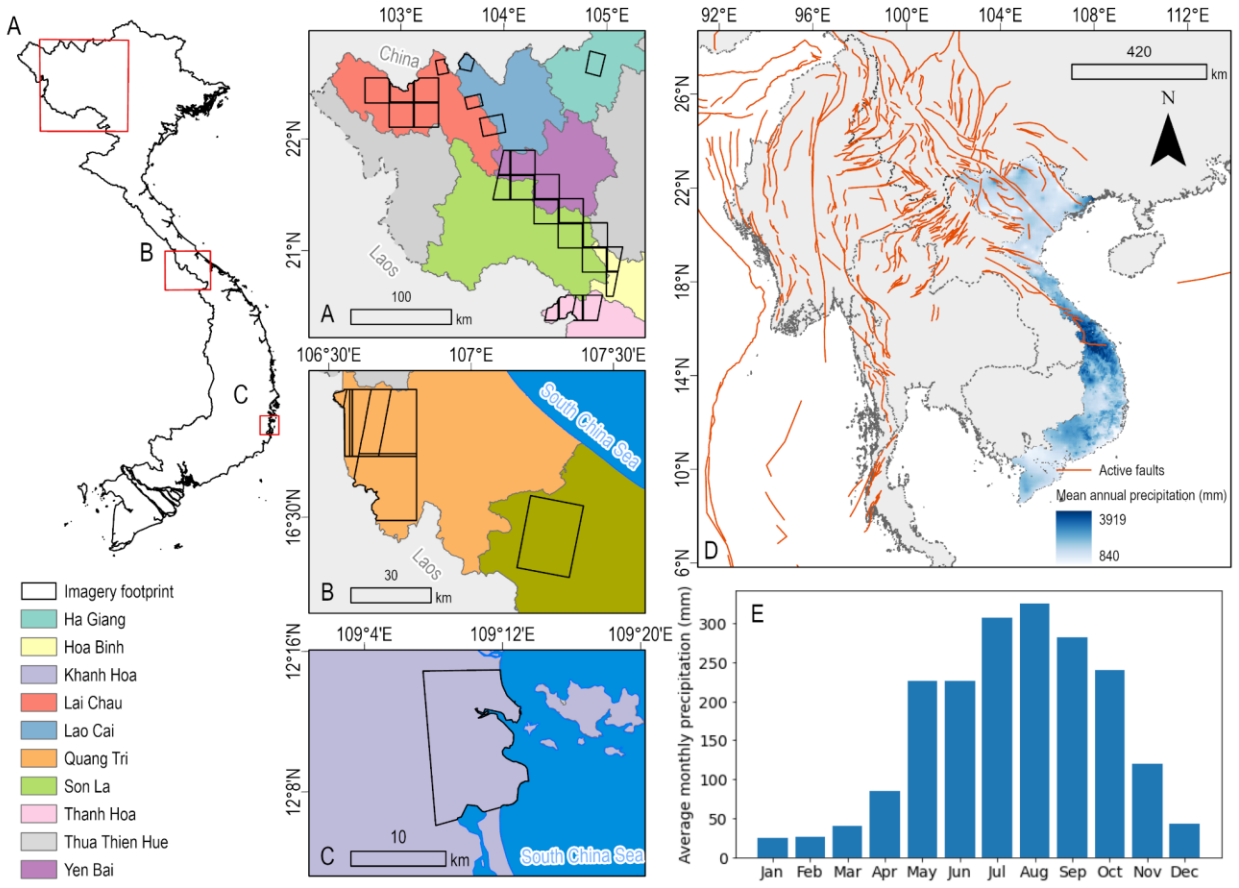

Figure 1. A-C. Study areas across Vietnam outlined in black, along with the provinces. D. Mean annual precipitation derived from Climate Hazards group Infrared Precipitation with Stations (CHIRPS) 1981-2021 with active faults from the Global Earthquake Model Foundation (GEM)

Active Faults database (Styron & Pagani, 2020). E. Average monthly rainfall derived from CHIRPS (1981-2021) over Vietnam.

3. Materials and Methods

3.1 Event-based landslide inventories

The original inventory on rainfall-triggered landslides used in this study traverses the Lower Mekong region, encompassing Cambodia, Myanmar, Laos, and Vietnam. It was generated using a semi-automatic landslide detection system built upon object-based methods. Areas affected by landslides were initially identified from news and official reports between 2009 and 2020. Landslides were then mapped automatically using NDVI changes derived from pre- and post-event imagery from PlanetScope and RapidEye (Lu et al., 2019). To enhance the accuracy, wrongly classified areas, including barren land and agricultural areas, were manually removed. The point locations in the inventory represent where the landslides initiated. For a detailed description of the exact methodology for generating the landslide inventory, we direct you to the original article by Amatya et al. (2022). Locations of all recorded landslide occurrences in Vietnam are shown in Figure 2.

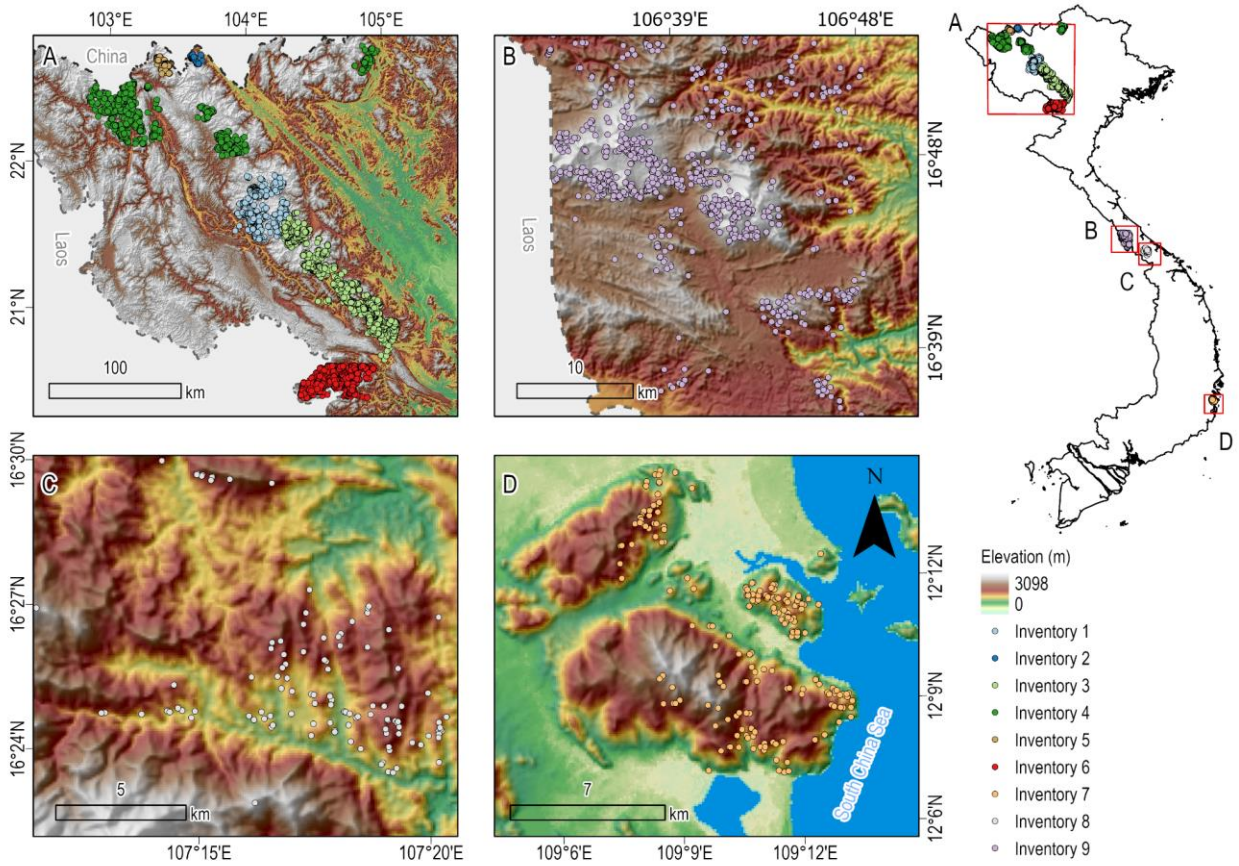

Figure 2. Landslide inventories mapped by Amateya et al. (2022) over Vietnam (point locations). The underlying topography corresponds to the elevation obtained from the Multi-Error-Removed Improved-Terrain (MERIT) DEM.

The indexing and number of landslide occurrences by date are shown in Table 3. The inventory has two shortcomings. Firstly, 9,008 out of the recorded 10,601 (85.0%) occurrences have some degree of temporal uncertainty ranging from 2 to 6 days; this refers to the precision to which the day of landslide events is assigned. Secondly, the time difference between pre- and post-event imagery is up to three years, with most image pairs used for mapping NDVI changes having slightly over a year's difference, potentially compromising the locational and temporal accuracy of these inventories. Due to these limitations, some assumptions were made in the way we treated the occurrence date of each landslide event. For records with temporal uncertainty, we assumed the latest date to be the reference day of landslide occurrence. This is a conservative choice because selecting the latest date ascertains that the signal of the rainfall trigger preceding the landslide event will be included in the analysis, whereas the earliest date may have omitted the rainfall trigger signal in some cases.

Table 3. Landslide inventory indexing by event dates and number of occurrences.

Inventory	Occurrence date	No. recorded landslides	Temporal uncertainty (days)
1	2/8/17 - 3/8/17	2,014	2
2	23/8/2017 - 28/8/2017	99	6
3	10/10/2017 - 11/10/2017	3,944	2
4	23/6/2018 - 24/6/2018	1,310	2
5	3/8/2018	302	0
6	27/8/2018 - 1/9/2018	1,641	6
7	18/11/2018	204	0
8	12/10/2020	116	0
9	18/10/2020	971	0

3.2 Mapping Units

Mapping units are a means of landscape partitioning. In the context of susceptibility modelling, a probability of slope failure is assigned to each unit. While early susceptibility studies often employed a grid cell structure for mapping units (Atkinson et al., 1998), alternatives such as hexagons (D’Ambrosio et al., 2003), administrative units (Zêzere et al., 2017), terrain units (Baeza

et al., 2010), unique condition units (Titti et al., 2021) and slope units (SUs) (Carrara et al., 1998) have been proposed in landslide susceptibility studies. SUs were chosen for our study because they satisfy the independence requirement between one landslide activation and the next. In other words, when a landslide occurs in a SU, its occurrence is independent or weakly dependent on a landslide in the adjacent SU (Yadav et al., 2023). SUs partition the terrain following drainage and catchment divide lines, aiming to maximise geomorphological homogeneity within each unit, and geomorphological differences between adjacent units (Alvioli et al., 2020). Additionally, studies based on SUs are less affected by positional errors associated with landslide mapping (Steger et al., 2016).

In this study, SUs were generated from the MERIT DEM using the open source *r.slopeunits* software (for details on software and methods see: Alvioli et al., 2016) in the areas extending up to a 30km buffer region outside the footprint of the satellite imagery used to map the landslides. Here, we parameterised *r.slopeunits* as follows: minimum surface area for the SU: 5,000,000m^2, circular variance: 0.2, threshold value for cleaning procedures: 300,000m^2, flow accumulation area threshold: 20,000,000m^2, reduction factor: 10, maximum surface area for the SU: 10,000,000m^2. Flat areas were removed during the automated delineation process since landslides cannot initiate there. Unreported tests on parameter sensitivity led to a partition of 4,525 SUs over the study area.

3.3 Predictors

The predictor variables used in our model can be broadly categorised into static and dynamic. Further details on each are presented in Sections 3.3.1 and 3.3.2 respectively. An overview of the data sources that were used to derive these variables is provided in Table 4.

Table 4. Information on the data used in our study. *SUs with landslide occurrences in 2020 were associated with the land cover of 2019.

Data	Source	Spatial resolution	Temporal resolution and period
Lithology	Hartmann & Moosdorf (2012)	1 : 3,750,000	NA
Land cover*	Buchhorn et al. (2020)	100m	Annual, 2015 – 2019
Active faults	Styron & Pagani (2020)	NA	NA
Elevation	Yamazaki et al. (2017)	90m	NA
Precipitation	Funk et al. (2015)	5,566m	Daily, 1981 – near present

3.3.1 Static conditioning factors

Conditioning factors – factors that may predispose a slope to failure – that were used in this study are shown in Table 5, along with the underlying rationale for their inclusion. These were selected because they are commonly-used conditioning factors in other landslide susceptibility studies (Reichenbach et al., 2018). For each SU, we derived the spatial mean and standard deviation of the continuous conditioning factors within each SU and the majority class for categorical conditioning factors. A detailed analysis of these conditioning factors is provided in the Supplementary Material. There, we showcase the distribution of covariates considered in this study and elaborate on tests performed prior to their inclusion in the model.

Table 5. Overview of static conditioning factors considered in the proposed study, and their underlying rationale.

Factor	Variable type	Rationale
Relief	Continuous	Shows uplift and erosion, most landslides are observed in areas with higher relief (Pareek et al., 2010).
Slope	Continuous	Steeper slopes are more susceptible to slope failure
Plane curvature	Continuous	Affects the convergence and dispersion of water movement
Profile curvature	Continuous	Affects acceleration of water movement (Oh & Pradhan, 2019)
Distance to nearest fault	Continuous	Landslides tend to occur near faults due to more extensive foliation and weaker shear strength of rock masses.
Cosine of slope aspect	Continuous	Quantifies influence of slope orientation. This is usually considered a proxy for the orientation of rock strata (Frattini et al., 2008) and sunlight exposition (Kouli et al., 2010).
Sine of slope aspect	Continuous	
Lithology	Categorical	Proxy for geo-technical properties which affect shear strength.
Land cover	Categorical	May predispose slopes to landslide occurrences and control the spatial distribution of landslides. The specific effects on shear stress and shear strength of the slope vary with land cover type.

3.3.2 Dynamic

Rainfall characteristics serve as the temporal and dynamic input to the models. Determining the most suitable temporal unit is more straightforward than its spatial counterpart because the

landslide inventories utilised in this study and rainfall from CHIRPS are both available at the daily scale. The rainfall parameters explored in this study are therefore the daily 1) sum *(S)* (Eq. 1), 2) max *(M),* cumulative sum *(CS)* (Eq. 2) 4) cumulative max *(CM)* (Eq. 3) and 5) sum difference *(SD)* (Eq. 4). To identify optimal time series length for our models, we tested time series for each parameter for series of 7, 14, 21 and 30 days, where the 30th day is the day of landslide occurrence. *S* represents the total amount of rainfall that falls within a SU, while *M* denotes the maximum rainfall value recorded based on the grid cells within the SU. On day 1, SD is assumed to be 0. These are derived according to the following equations, where *n* refers to the number of days in the rainfall time series:

$$S_n = \sum_{i=1}^{n} \quad pixel\ value \cdot fraction\ of\ SU\ overlap\ with\ pixel \qquad \text{(Eq. 1)}$$

$$CS_n = CS_{n-1} + S_n \qquad \text{(Eq. 2)}$$

$$CM_n = CM_{n-1} + M \qquad \text{(Eq. 3)}$$

$$SD_n = S_n - S_{n-1} \qquad \text{(Eq. 4)}$$

With the intention of building a model that discriminates between landslides and non-landslide occurrences in SUs with high possibilities of slope failure, we excluded SUs with minimal to no rainfall. Analogous to the exclusion of flat areas in the SU generation process, our models were trained using SUs that experienced intense rainfall in the 30-day time period (further elaboration on the selection procedure is provided below). The goal was to avoid the model from converging towards a simplistic solution where it associates non-occurrences with no rainfall, and vice versa.

To filter out SUs that did not experience intense rainfall, we initially examined the rainfall distribution of SUs with landslides and determined the 95th percentile of *M* and *S* for SUs associated with landslide presences in the 30 days of rainfall. Subsequently, SUs associated with landslide absences where *M* or *S* did not have at least one day with rainfall more than or equal to the 95th percentile were excluded. This was done to exclude SUs with minimal to no rainfall, such that our model would only be trained on SUs that experienced intense rainfall. This was done to avoid having the model converge towards a trivial solution, whereby non-occurrences are associated with no rainfall, and vice versa. With this, a total of 2,759 SUs were selected for this study, with 1,572 absences and 1,172 presences. The number of SUs with landslide presences have been significantly reduced because multiple landslides could have occurred in a single SU.

The time series of rainfall variables for the considered SUs in this study are presented in Figure 4 in the form of summary statistics and a kernel density estimate (KDE) plot. Rainfall parameters between landslide and non-landslide SUs seem nearly identical, with differences in rainfall readings at the decimal scale. This alignment with our expectations is attributed to our study being conducted at a relatively small local scale, whereas CHIRPS has a coarse spatial resolution of 5,000m. While immediate differences in rainfall patterns between rainfall and non-rainfall SUs cannot be observed, certain NN can recognise small signal differences between two time series.

For this reason, we chose to use a model architecture capable of processing the rainfall time series. Further elaboration on the model architecture is provided in Section 3.5.

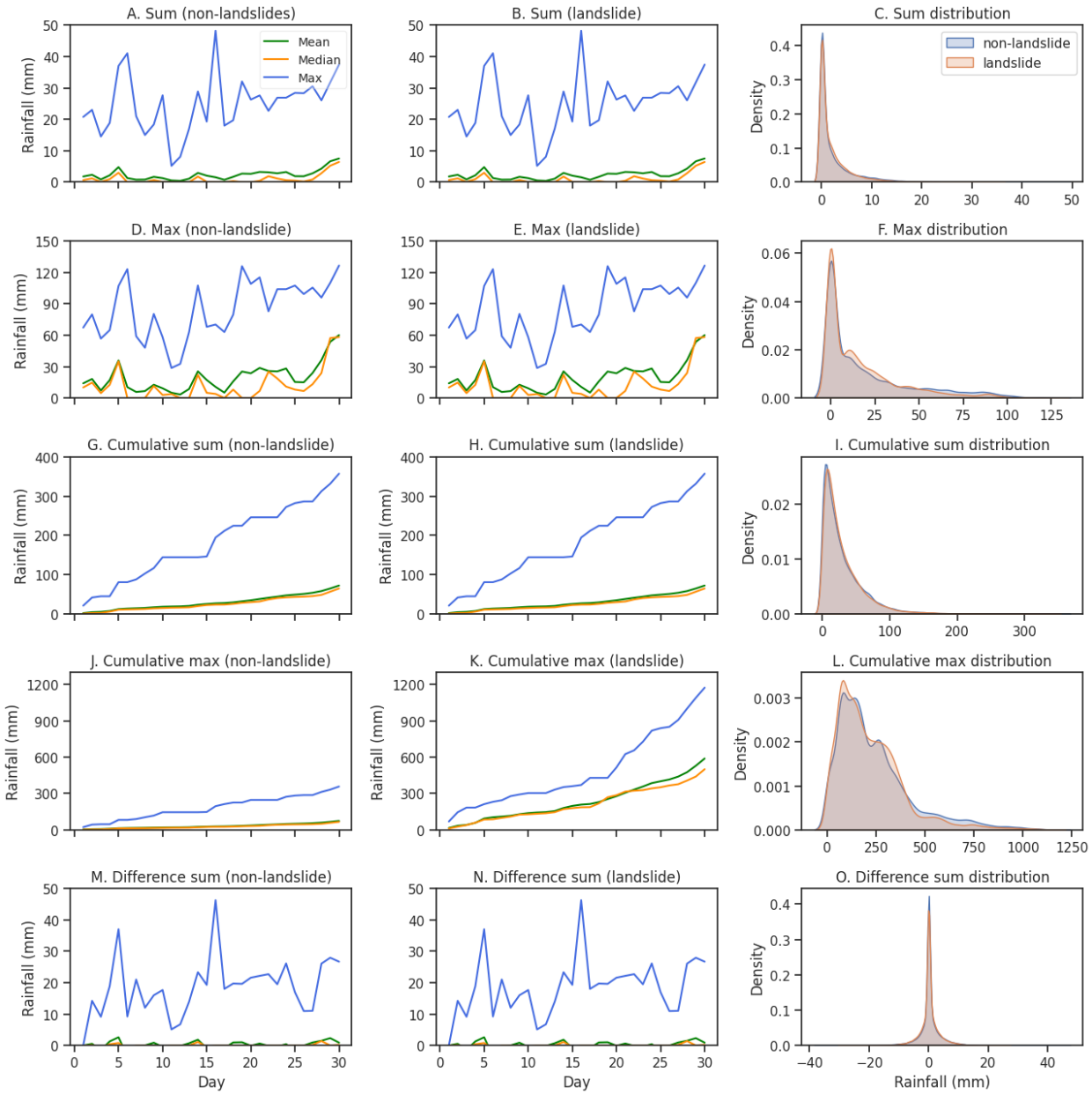

Figure 4. Summary statistics on rainfall parameters that were analysed in this study, averaged for all selected non-landslide SUs (left column) and landslide SUs (right column). KDE plots in the right column comprise data from all SUs (i.e. both landslide and non-landslide SUs).

3.4 Pre-processing of covariates

Pre-processing – specifically normalising or standardising – of covariates and rainfall data was carried out prior to the modelling phase to enhance model convergence. Additionally, this ensures

equal treatment of all features during the learning process. The continuous environmental variables were normalised and scaled as follows:

$$Z\text{-}Score = \frac{Original\ value - mean\ covariate\ value}{Standard\ deviation\ of\ covariate} \quad \text{(Eq. 5)}$$

Concerning pre-processing of rainfall, four different methods were employed in this study to explore how they affect model performances. While we only refer to the combination of z-scoring (Eq. 5), as well as the minimum-maximum scaler (Eq. 6) in the results section, all experiments utilising other pre-processing methods are detailed in the Supplementary Material, Table 3.

$$Scaled\ value = \frac{Original\ value - minimum\ value}{Maximum\ value - Minimum\ value} \quad \text{(Eq. 6)}$$

3.5 Modelling Framework

3.5.1 Dataset split

Out of the 2,759 retained SU samples (Section 3.3.2), 2,069 (75%) were used for hyperparameterization, of which 1,655 (60%) were used for training and 414 (15%) were used for validation. Thereafter, this same 75% of SUs used in the hyperparameterization were used to train the model, while the remaining 25% of unseen data was set aside for validation in the initial stage of selecting the best model based on the 30-day time series of rainfall. A pre-determined seed was set to ensure that the randomisation used to divide the dataset into training, validation, and test sets was consistent across multiple runs.

3.5.2 Hyperparameter tuning

With the aim of creating a fully automated modelling framework, we sought to optimise the hyperparameters using the Hyperband and Bayesian optimization algorithms using the validation area under the curve (AUC) as the objective function. Specifics on the hyperparameters that were optimised is found in the Supplementary Material. These algorithms are available from the Keras Tuner Library (O'malley et al., 2019). The Hyperband Algorithm (Li et al., 2017) combines the benefits of a Random Search algorithm (Bergstra & Bengio, 2012) and successive halving (Jamieson & Talwalkar, 2016) to efficiently elucidate the best set of hyperparameters. The algorithm works by dividing the available computation budget into multiple rounds, where each round consists of multiple iterations of training and evaluation. A fraction of best-performing hyperparameters is retained for further testing in the next round, with more computational resources being allocated (i.e. more iterations and more data).

In contrast to the Hyperband algorithm, which involves point-wise evaluations of an objective function, a Bayesian Optimization (Snoek et al., 2012) approach limits the number of such computationally expensive evaluations. This is done by creating a probabilistic model which incorporates all prior assumptions associated with the objective function to be optimised. This

model is then used to select the next set of hyperparameters to be evaluated. It is then updated with each iteration. After a certain number of iterations is done, the hyperparameters which yielded the best performance are selected.

3.5.3 Overfitting

Overfitting in DL happens when the performance on the validation dataset is significantly worse than on the training set due to the model fitting too well on the training data, such that it has lost its capability to generalise to unseen data. In the context of NNs, this happens due to complexity from the large number of parameters. To prevent this, batch normalisation (Ioffe & Szegedy, 2015) and dropout layers (Srivastava et al., 2014) were introduced in the modelling framework. Batch normalisation stabilises and speeds up the training process while having a regularisation effect, thereby helping to reduce overfitting. On the other hand, dropout layers also have a regularisation effect by randomly forcing a fraction of the NN neurons to zero during each training iteration. This prevents the NN from relying heavily on specific features or neurons.

3.5.4 Learning algorithms

Optimizer functions are used during the training process of the NN and play a crucial role in updating the weights and biases of NNs. The Adam optimizer (Kingma & Ba, 2014) was selected in this study for the following reasons: 1) its ability to adapt learning rates, thereby making it suitable for a wide range of problems without having to tune learning rates extensively, 2) its robustness to noisy gradients, and 3) its relatively faster convergence speed compared to traditional algorithms such as the Stochastic Gradient Descent (Ruder, 2016).

3.5.5 Modelling framework

NNs are general non-linear function approximators that have been extensively used for classification and pattern recognition problems due to their demonstrated ability in the forecasting of complex dynamic non-linear systems. They have several advantages over conventional probabilistic methods and machine learning methods, such as Logistic Regression (Cox, 1958), Random Trees (Lavalle, 1998), Support Vector Machine (Cortes & Vapnik, 1995). This includes independence from the statistical distribution of the data (Lee et al., 2004), the flexibility of collectively using categorical and numerical data (Kawabata & Bandibas, 2009) and the ability to comprehend complex, non-linear relationships between variables.

The modelling framework employed in this study is shown in Figure 5. The spatial component uses static terrain characteristics as input into a Fully Connected Neural Network (FCNN), while the temporal component is made up of a GRU. The 30-day rainfall time series is fed into the GRU. The outputs of these two components serve as inputs into a second FCNN. This specific construction was chosen to ensure that the features from the spatial and temporal components

are allowed to interact with each other, and thus produce a prediction based on information from both components.

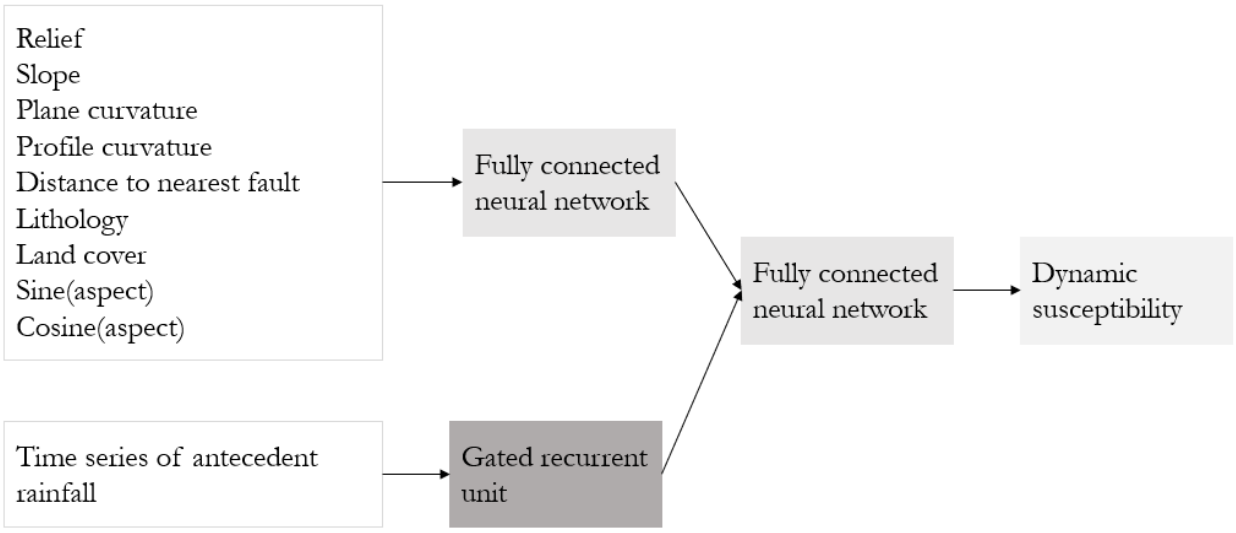

Figure 5. Conceptual sketch of the model employed in this study.

All modelling experiments followed a consistent sequence: terrain and rainfall variables were first pre-processed – this involved normalisation or scaling, as per experiment specifics. Subsequently, automated hyperparameterization determined the optimal set of hyperparameters for model training. As described in Section 3.5.1, the model is trained using the same 75% of the data that was used during the hyperparameterization phase, and its performance is tested using the remaining 25% of unseen data. The performance metric used is the Area under the Curve (AUC) of the Receiver Operating Characteristic (ROC) Curve, and is further elaborated on in Section 3.6. After conducting multiple experiments and comparing the validation performance based on the 25% of unseen data, the best-performing model underwent a 10-fold cross-validation to evaluate its performance and generalizability. The 10-fold cross validation was done with mutually exclusive subsets, collectively covering the entire dataset.

Following this, further experiments using the best model were done to determine the optimal antecedent rainfall window (i.e. the number of days of rainfall which should be used as the model input). Three more experiments were done, whereby the number of days of antecedent rainfall used were 7 days, 14 days and 21 days. This is where the difference between a traditional LEWS and our approach is particularly evident – the former makes use of a single scalar value irrespective of the length of the time window, while the latter introduces a proportionally longer time series based on the window size used (7 days = 7 data points, 14 day = 14 data points, etc.). The same procedure of pre-processing and hyperparameterization as above was carried out. Among these three trials, the model with the best performance (measured by validation AUC), as well as the 30 day model counterpart, was then subjected to a further 10-fold cross validation.

3.6 Performance assessment

The performance metric used in this study is the AUC of the ROC curve. This graphically illustrates the trade-off between sensitivity and specificity as the discrimination threshold of a binary classifier is adjusted. The AUC quantifies the overall performance across all possible discrimination thresholds. AUC values range between 0 to 1, with 1 being a perfect classifier, while 0.5 being a random classifier.

To align with the labels in our data (i.e. landslide presences or absences), we converted the output probabilistic values from our models into binary labels using a threshold. It is crucial to acknowledge that the optimal threshold is problem-specific and involves a trade-off between evaluation metrics and a balance between False Positives (FP) and False Negatives (FN). In this study, the Youden's Index *(Y)* (Youden, 1950) was used to derive the thresholds used for assigning labels to the output probabilities from the modelling phase. Mathematically, *Y* represents the difference between True Positive Rate (TPR) and False Positive Rate (FPR). These indicate instances where landslides were respectively correctly and incorrectly predicted. The optimal threshold is where this difference is maximised. The expression for this index is as follows:

$$\textit{Youden Index (Y)} = \frac{True\ positives}{True\ positives + False\ negatives} + \frac{True\ negatives}{True\ negatives + False\ positives} - 1$$

3.7 Benchmark

To establish a basis of comparison for our method against the conventional practice of using a single scalar representation of rainfall, we conducted a benchmark run. In this run, we substituted the entire time series for rainfall in the GRU component – which handles the temporal aspect of the model – with a scalar representation of the rainfall time series (*i.e.* the last rainfall reading for *CS*). All other variables, such as pre-processing methods and modelling framework were kept consistent.

4. Results

4.1 Performance overview

The best validation AUC results from the initial round of experiments involving the 30-day antecedent rainfall was antecedent rainfall was 0.795. This experiment set up was retained and subjected to further trials, varying the antecedent rainfall window as detailed in Section 3.5. Among the tested periods, a 14-day antecedent rainfall window was found to be optimal. The summary statistics of the AUC values for both the 14-day and 30-day variants are presented in Table 6. Both models perform comparably across all metrics, indicating good consistency. The standard deviation of AUC for the 30-day trial is slightly higher than the 14-day trial.

Table 6. Summary statistics for the 10-fold cross validation AUC of the 14-days and 30-days trials.

	10-fold cross validation AUC					
Antecedent rainfall window (days)	Mean	Median	Max	Min	Range	Std
14	0.780	0.779	0.806	0.751	0.055	0.0164
30	0.781	0.779	0.809	0.750	0.058	0.0182

4.2 Classification accuracy

The probabilistic output of the models was translated into confusion maps as shown in Figures 6 and 7 for the 14-day and 30-day models, respectively. Such maps convey the result of the confusion matrix spatially. For a confusion matrix to be computed, a probability cut-off has to be selected, here determined by the Youden Index. Notably, the 30-day variant has a slightly higher accuracy (70.9%) than the 14-day variant (69.7%). For the 30-day model, 55.3% of these correct predictions originate from True Negatives (TN), which refer to correct predictions of non-landslide occurrences. This stands at 47.5% for the 14-day model. The distribution of False Negatives (FN) and TP is more balanced in the 14-day model (see Figures 6F and 7F). Geographically, the four elements of the confusion map exhibit considerable similarity between both variants for the panels A, B and C shown in Figures 6 and 7. Similar to what was observed in Section 4.1, the two models produce analogous results. Looking at the classification patterns, few differences can be observed in the way TN, TP, FN and FP are recognised in both cases. These differences will be further discussed in Section 5.

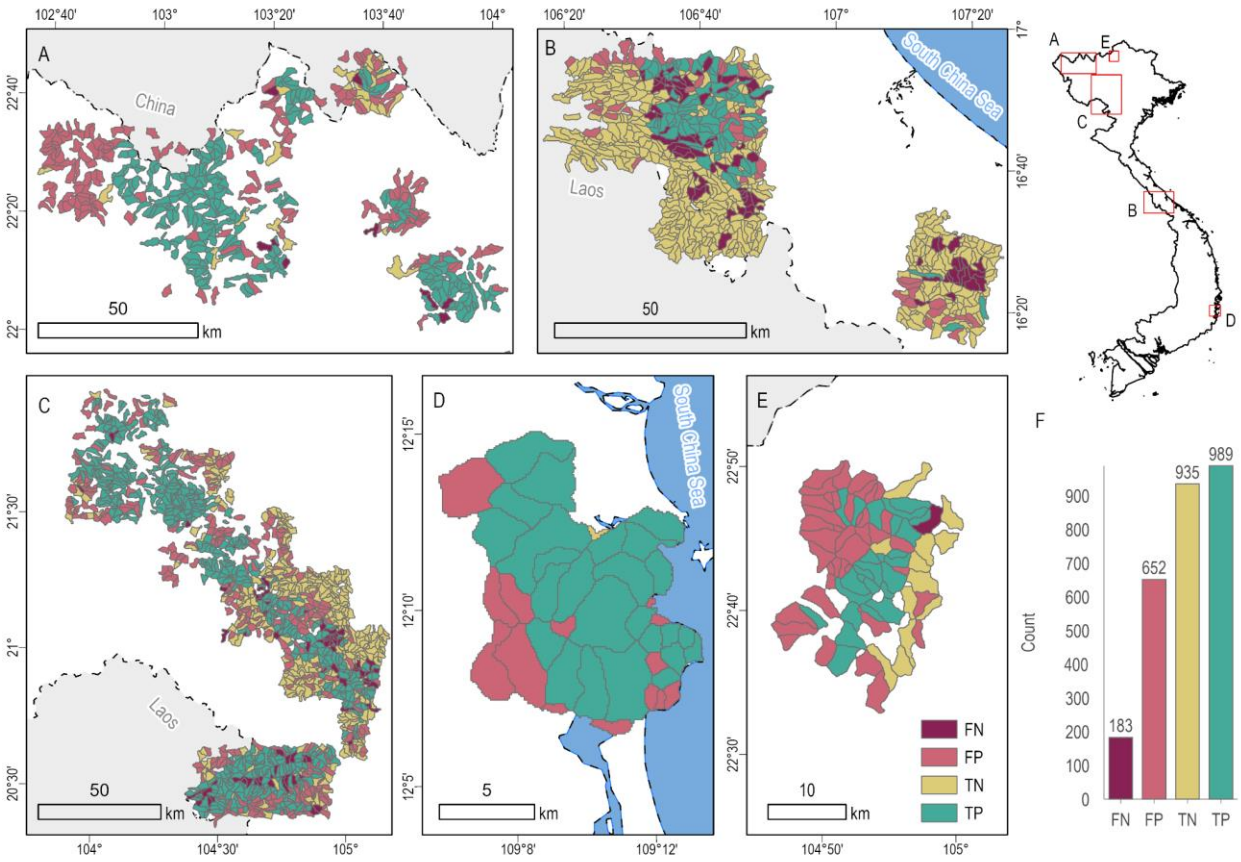

Figure 6. Confusion map for the 14-days model. This map shows the four elements of the confusion matrix across the geographic space.

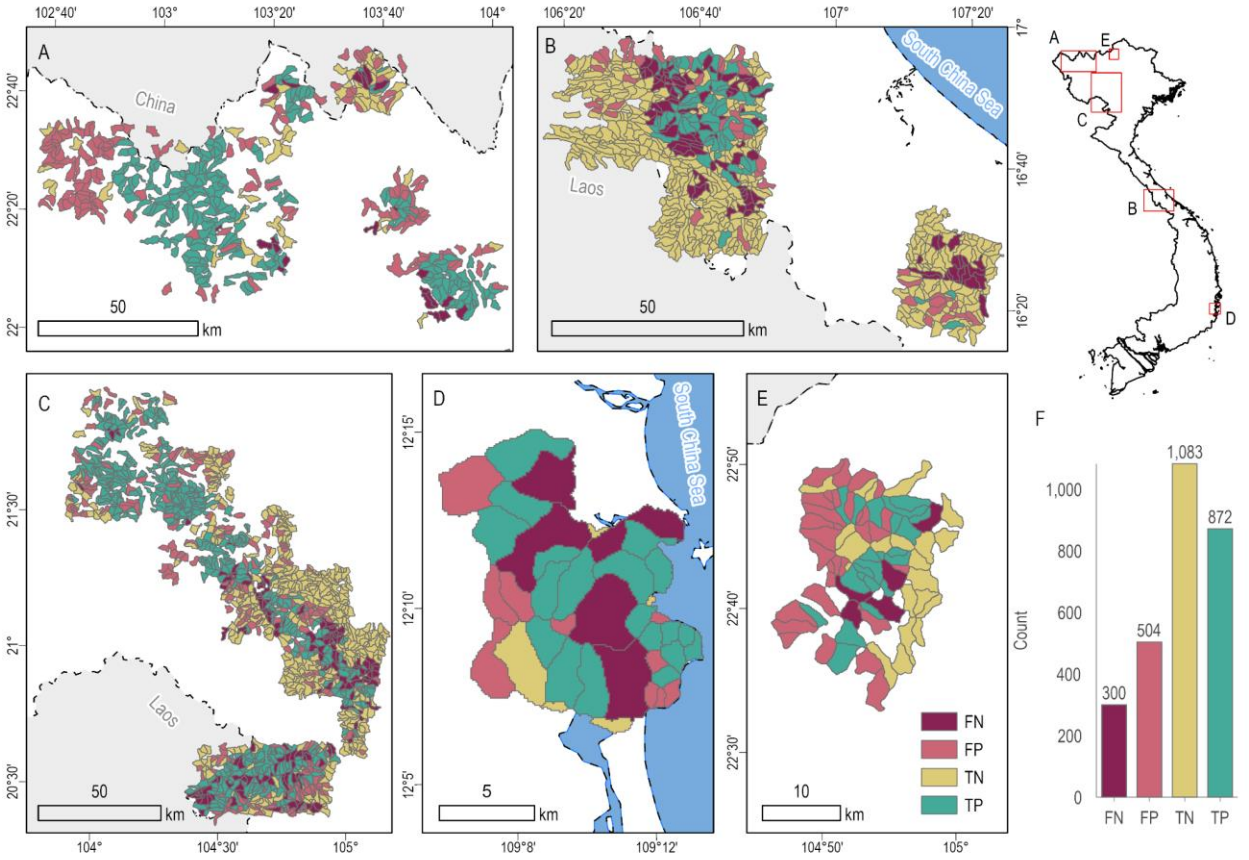

Figure 7. Confusion map for the 30 day model. This map shows the four elements of the confusion matrix across the geographic space.

To further segment the performance metrics at the inventory level in Figures 8 and 9, we report the confusion metrics per landslide event. The accuracy for the 14-day model ranges from 53.4% to 79.0% across inventories, while the 30-day model ranges from 57.7% to 78.0%. Notably, the 14-day model shows its weakest performance (< 60% accuracy) for inventories 2, 4 and 6, in descending order. The 30-day model shows poorest performances for inventories 6, 7 and 4, in descending order. The results are in line with the expectations that model performance is the worst for inventories with high temporal uncertainty – specifically 6 days for inventories 2 and 6. Conversely, the best performances are generally observed in the inventories with the lowest temporal uncertainty, such as inventories 8 and 9. In these cases, the models achieved at least 77% accuracy.

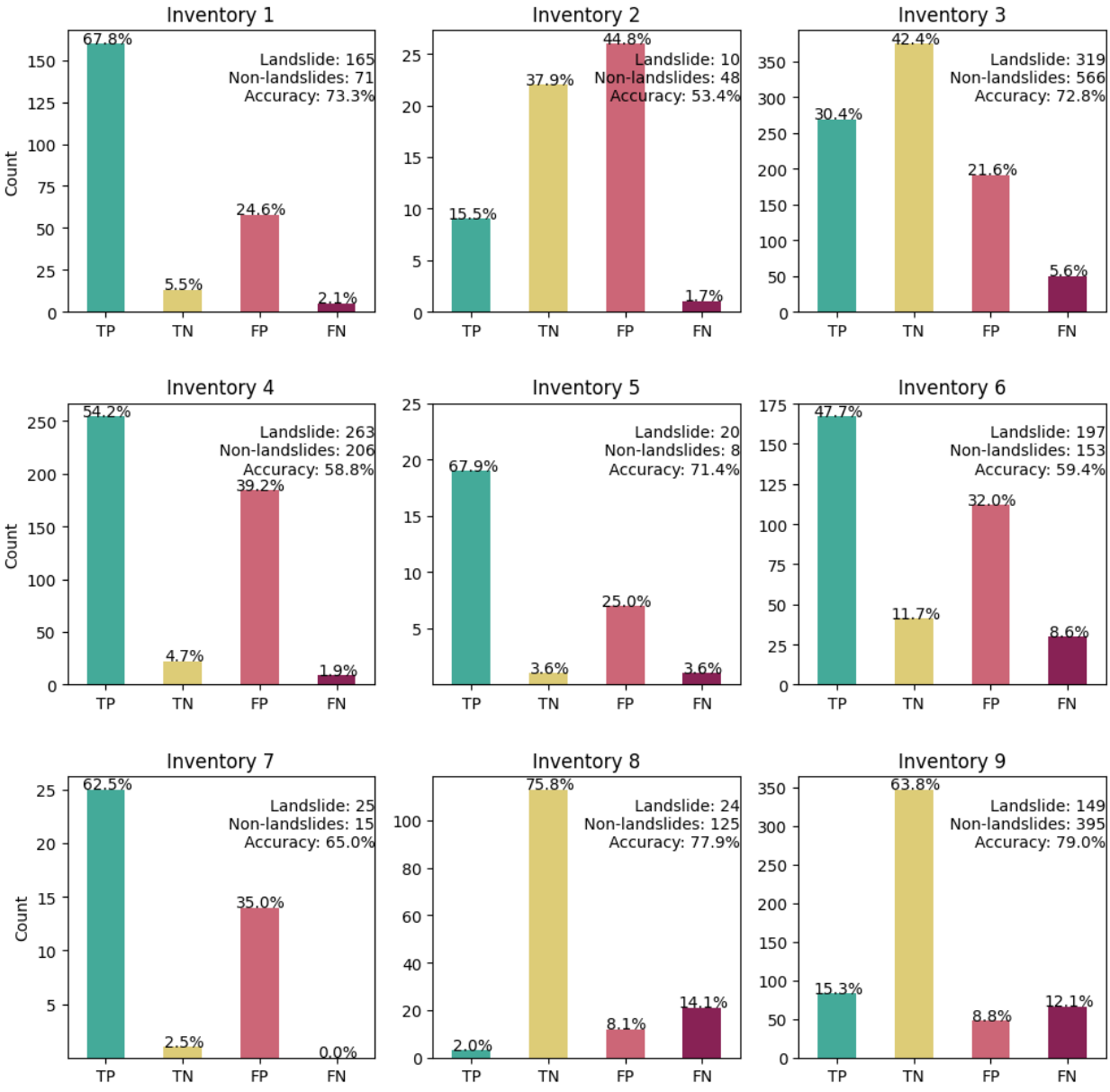

Figure 8. Confusion matrix results by inventory for the 14-day model.

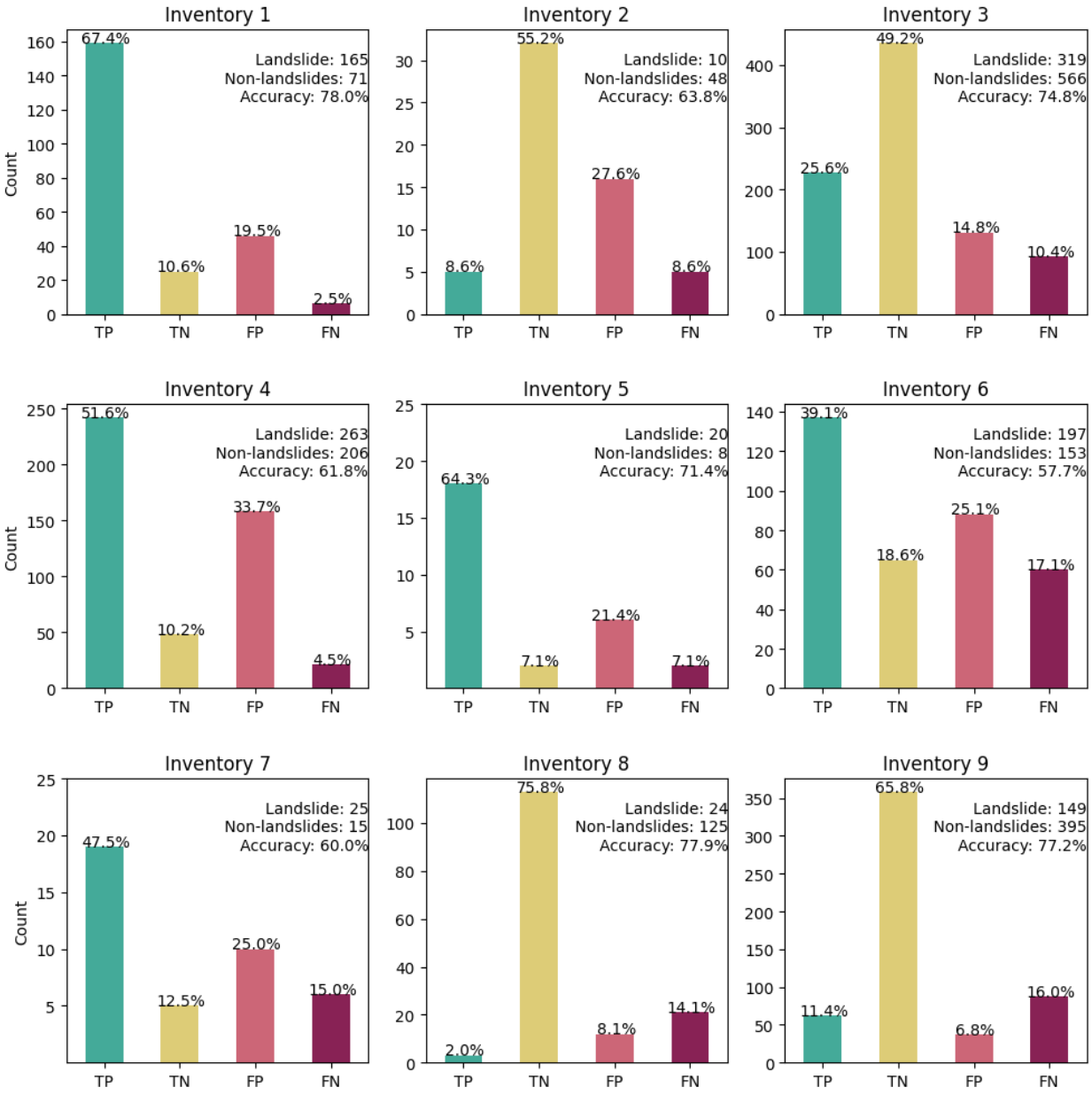

Figure 9. Confusion matrix results by inventory for the 30-day model.

4.3 Model benchmark

The ROC curves from the 10-fold cross validation for the ‘best’ time series model (A) and the baseline run (B) are depicted in Figure 10. The boxplot of AUC values illustrates that our approach, utilising the entire time series, yields superior results compared to the traditional single scalar value approach in the hindcasting of landslides. The median is AUC of 0.78 against 0.69 for the benchmark, each with a 95% confidence interval of 0.06. The AUC difference is significant with the two boxplots never intersecting in any of the cross-validation runs.

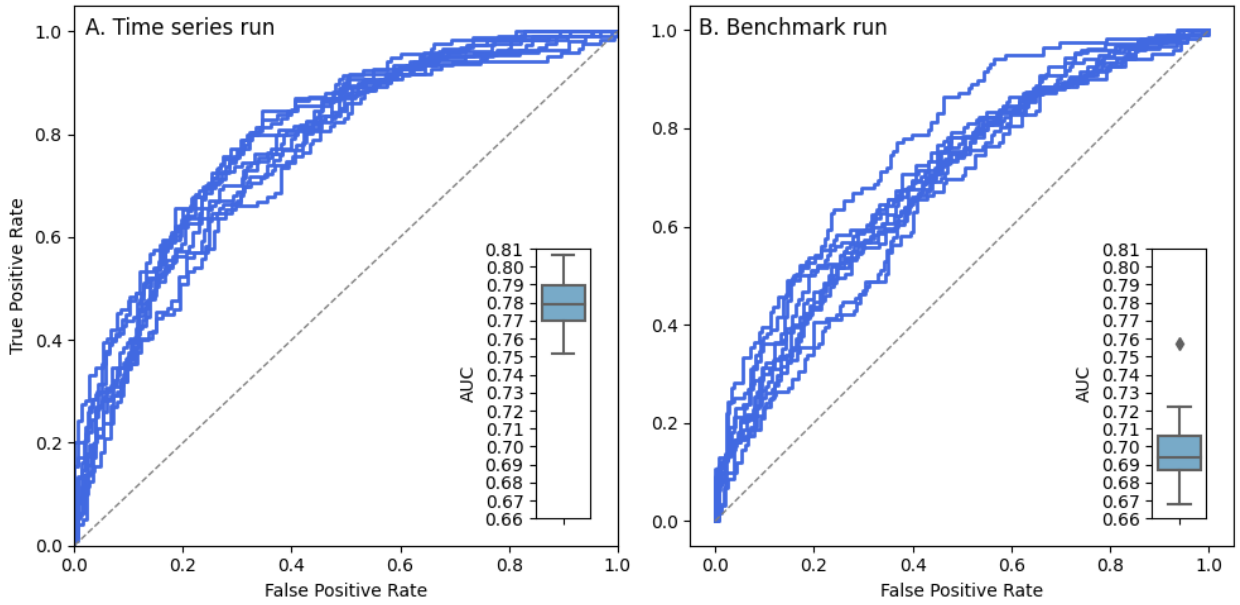

Figure 10. A. 10-fold cross validation ROC curve from the 14-day trial (functional use of rainfall parameters). AUC values range from ~0.75 to ~0.81. B. 10-fold cross validation ROC curve from the benchmark trial (scalar use of *CS* rainfall). AUC values range from ~0.67 to ~0.72.

4.4 Considerations for model performances

Out of the 11 variations of our 30-day model, including covariates and associated scaling or normalisation techniques, we selected one structure that was further tested with rainfall antecedent windows of 7, 14, and 21 days. The reference 30-day model and the 14-day one produced the highest prediction skill which we examined from three perspectives: 1) the aggregated level using ROC curves, 2) the spatial level through confusion maps, and 3) the individual inventory level via confusion matrices. This performance overview showcased limited variation between the 14 and 30-day models. Therefore, we consider the 14-day model our best based on both methodological and operational considerations. Methodologically, one usually seeks to minimise complexity while maintaining the same performance. In our case, the additional information brought by including the rainfall signal from the 15th to 30th day had negligible effects. Hence, we selected the model with the shortest time window. A shorter time window also minimises computational time that our model would require to produce dynamic susceptibility estimates on a daily basis.

The confusion maps resulting from the two models are similar, albeit with some differences. The 14-day model produces a 6.6% FN, 23.6% FP, 33.9% TN and 35.8% TP, while the 30-day model produces 10.9% FN, 18.3% FP, 39.3% TN and 31.6% TP. We consider the ability to predict TPs (i.e. correctly predict the occurrence of a landslide) to be most important since they cause the most damage and disruption. The 14-day model outperforms the 30-day model by 4.2%, therefore being our best. Specifically, the latter produces 10.9% FN, as compared to the 6.6% generated by our 14-day model, which, if assumed as a basis for a LEWS, would lead to more conservative warnings (less prone to Type II errors). In other words, a higher FN implies that a given

susceptibility in space and time is underestimated. Thus, one would favour a LEWS that minimises the number of FNs since it avoids recommending locals to behave as usual in a condition of probabilistic landslide threat. Conversely, the 30-day model outperforms its 14-day counterpart in terms of FP; the more acceptable error.

Further breaking down the comparison at a much more localised scale, the two models underscore the crucial role of landslide inventory quality and completeness (Guzzetti et al., 2012; Tanyaş & Lombardo, 2020). These directly affect the reliability of landslide susceptibility modelling. This point is exemplified by the variability of model performance by inventory (Figures 8, 9). There, we see better performances (accuracy consistently above 65%) associated with inventories with lower temporal uncertainty (confined between 0 to 2 days). On the contrary, cases with temporal uncertainties up to 6 days produced larger misclassifications (accuracy below 60%).

Our best model is also benchmarked against a standard structure where the rainfall signal is compressed into a single scalar value, computed over the 14-day time window. This time, performance differences appear significantly larger in terms of the range of AUC obtained through a 10-fold cross validation routine. Our 14-day model suitably predicts landslides with AUC ranging approximately from 0.75 to 0.81, while the benchmark ranges between roughly 0.67 to 0.72. Notably, one cross validation run out of 10, constitutes an outlier of approximately 0.76 AUC, roughly the minimum obtained through our best model.

5. Discussion

The first scientific contribution that established a minimum rainfall threshold responsible for widespread landsliding goes back to Endo (1969). While significant advances have been made since then, the core structure of a LEWS remained unchanged – early warnings are issued on the basis of a spatio-temporal model that relies on a scalar representation of the rainfall signal. Here, we introduce an alternative based on three recent studies by Fang et al. (2023), Moreno et al. (2023) and Ahmed et al. (2023). The first paper proposed treating rainfall as a continuous signal rather than simplifying it in a single value. The second proposed modelling dynamic susceptibility based on covariates related to a scalar representation of rainfall and terrain properties in a data-rich context (Italian Alps), while the third used a similar modelling structure but tested it in a data-scarce context, Vietnam.

We partitioned our study area into SUs and dynamically estimated susceptibility based on static and dynamic predictors, with the former being terrain characteristics, and the latter being a continuous temporal rainfall signal captured by the GRU. The novelty of our approach lies in the combined use of rainfall time series with additional spatial predictors. The results indicate that our approach outperforms the traditional scalar benchmark, raising the question of how our approach could be operationalized into a LEWS. One of the clear strengths is the exclusive use of open data. The landslide inventory was openly shared by Amateya et al. (2022), and this practice of sharing data is only expected to increase in the coming years. In fact, automated mapping tools are increasingly ubiquitous. DL architectures are regularly used to produce landslide inventories in space and time (Bhuyan et al., 2023, Novellino et al., 2024) while discriminating between landslide types (Rana et al., 2023) and the likely trigger (Rana et al., 2021). These tools are also

frequently published openly to promote the benchmarking against same procedures in a consistent manner (Amateya et al., 2021; Das et al., 2023; Rana et al., 2022), thus encouraging the adoption and enhancement of the developed approaches.

Nonetheless, automated landslide mapping protocols still have limitations, the most significant being inaccurate time attribution of landslide occurrences. In fact, this affects most existing landslide studies. Based on the example from Amatya et al. (2021), the consistent global acquisition of optical images allows for the generation of landslide inventories with a relatively narrow temporal uncertainty. However, our model performance implies that temporal uncertainty still led to errors in the dynamic susceptibility assessment. A recent study (Dejins et al., 2023) further explored the combined use of optical images to map landslides and synthetic aperture radar analysis to constrain even more the occurrence time by means of assessing signal coherence and detrended coherence. The authors report narrowing down the temporal uncertainty to a range of 1 to 49 days. Therefore, if further refined, such an approach could eventually produce landslide inventories with reliable dating for modelling purposes.

Theoretically, a model trained on globally available data could be transferred from one area to another. This is supported by global landslide inventories and predictors such as DEMs, land cover maps (Brown et al., 2022), lithology (Hartmann & Moosdorf, 2012), soil (Poggio et al., 2021), and climatic variables (Funk et al., 2015; Huffman et al., 2015). In reality local models may not be easily generalizable. For instance, our used data source for rainfall (CHIRPS) can only be used for hindcasting purposes, but not forecasting. If we would explore the operational use of our model, forecasted rainfall should be used as the input. This would come with further complexities – for instance, GPM IMERG (Huffman et al., 2015) provides rainfall forecasts every 3-hours, although at the expense of the spatial resolution (~11km as opposed to ~5km from CHIRPS). Its finer temporal resolution brings more information as compared to CHIRPS, which only provides a daily description of the rainfall. The use of GPM-IMERG could enable a more in-depth investigation of the advantages of our full time series approach because the spatio-temporal signal of rainfall would be eight times richer. Therefore, one could check whether a finer rainfall description could lead to better landslide predictions, taking advantage of a better description of peak intensities.

Keeping the reflections on the extension towards IMERG, such products typically miss extreme rainfall values as compared to *in-situ* measurements (Gupta et al., 2020; AghaKouchak et al., 2011). Thus, if one would envision using forecasted rainfall, regardless of the source, it could be beneficial, if not a requirement, to introduce an intermediate bias correction step. In other words, a model could be trained to find a match between rain gauge and satellite rainfall products, thereby adjusting the forecast prior to its use for landslide prediction. This could go alongside a parallel downscaling step (e.g. modern super resolution techniques (Sharma et al., 2022)) to adapt the ~11km grid size at the scale compatible with spatio-temporal landslide initiation processes.

Aside from data-related considerations, improvements could also be made in terms of the modelling architecture. For example, our choice of a GRU implicitly constrained the importance

of rainfall to exponentially decay backwards with time from the landslide date. This is certainly a reasonable assumption, as even in the literature, the rainfall contribution to slope failures is referred to triggering (on the day of the event) and preparatory (before the event) (Steger et al., 2022). In reality, this assumption may be invalid since this decay might not follow an exponential decline. Therefore, alternatives such as Transformer Neural Networks (Han et al., 2021), where an attention mechanism (Vaswani et al., 2017) flexibly recognises important segments of a time series independently of the relative positions, might be more suitable for further studies.

6. Concluding remarks

Models that are capable of capturing the continuous effect of the rainfall time series may shape the future of LEWS. Besides relying solely on rainfall information, such models should also incorporate landscape characteristics. This is demonstrated in our work, taking Vietnam as an example, where our model outperformed the standard use of a single cumulative rainfall measure for predicting landslide occurrence. Our research expands on space-time prediction of rainfall-induced landslides through the use of NNs that were originally designed for speech recognition. We envision future experiments that address two areas of improvement: incorporating forecasted rainfall products, and using joint models whose architecture allows for the estimation of susceptibility and intensity, where intensity is a proxy for landslide size (area, volume, relative densities per mapping unit of choice). If both areas of improvement would lead to positive results, we envision a potential LEWS capable of fully describing the landslide hazard as a function of landscape and spatio-temporal characteristics of rainfall.

Acknowledgements

This research was funded under Deltares' Enabling Technologies and SiTO programmes.

Author contributions

Jana Lim: Conceptualization, Data curation, Formal analysis, Investigation, Methodology, Validation, Visualization, Writing – Original draft, Writing – review & editing, Visualization. **Giorgio Santinelli:** Funding acquisition, Supervision, Writing – review & editing. **Ashok Dahal:** Methodology. **Anton Vrieling:** Supervision, Writing – review & editing. **Luigi Lombardo:** Conceptualization, Methodology, Supervision, Writing - Original draft preparation, review and editing.

References

Ahmed, M., Tanyas, H., Huser, R., Dahal, A., Titti, G., Borgatti, L., Francioni, M. & Lombardo, L. (2023). Dynamic rainfall-induced landslide susceptibility: a step towards a unified forecasting system. *International Journal of Applied Earth Observation and Geoinformation*, *125*, 103593.

AghaKouchak, A., Behrangi, A., Sorooshian, S., Hsu, K., & Amitai, E. (2011). Evaluation of satellite-retrieved extreme precipitation rates across the central United States. *Journal of Geophysical Research: Atmospheres*, *116*(D2).

Alvioli, M., Marchesini, I., Reichenbach, P., Rossi, M., Ardizzone, F., Fiorucci, F., & Guzzetti, F. (2016). Automatic delineation of geomorphological slope units with r. slopeunits v1. 0 and their optimization for landslide susceptibility modeling. *Geoscientific Model Development*, *9*(11), 3975-3991.

Alvioli, M., Guzzetti, F., & Marchesini, I. (2020). Parameter-free delineation of slope units and terrain subdivision of Italy. *Geomorphology*, *358*, 107124.

Amatya, P., Kirschbaum, D., Stanley, T., & Tanyas, H. (2021). Landslide mapping using object-based image analysis and open source tools. *Engineering Geology*, 282, 106000.

Amatya, P., Kirschbaum, D., & Stanley, T. (2022). Rainfall-induced landslide inventories for Lower Mekong based on Planet imagery and a semi-automatic mapping method. *Geoscience Data Journal*, *9*(2), 315-327.

Atkinson, P., Jiskoot, H., Massari, R., & Murray, T. (1998). Generalized linear modelling in geomorphology. *Earth Surface Processes and Landforms: The Journal of the British Geomorphological Group*, 23(13), 1185-1195.

Baeza, C., Lantada, N., & Moya, J. (2010). Influence of sample and terrain unit on landslide susceptibility assessment at La Pobla de Lillet, Eastern Pyrenees, Spain. *Environmental Earth Sciences*, 60, 155-167.

Bergstra, J., & Bengio, Y. (2012). Random search for hyper-parameter optimization. *Journal of Machine Learning Research*, *13*(2).

Bhuyan, K., Tanyaş, H., Nava, L., Puliero, S., Meena, S. R., Floris, M., van Westen, C. & Catani, F. (2023). Generating multi-temporal landslide inventories through a general deep transfer learning strategy using HR EO data. *Scientific report*s, 13(1), 162.

Bien, T. X., Iqbal, M., Jamal, A., Nguyen, D. D., Van Phong, T., Costache, R., Ho, S. H., Le, H. V., Nguyen, H. B. T., Prakash, I. & Pham, B. T. (2023). Integration of rotation forest and multiboost ensemble methods with forest by penalizing attributes for spatial prediction of

landslide susceptible areas. *Stochastic Environmental Research and Risk Assessment*, 1-20.

Buchhorn, M., Lesiv, M., Tsendbazar, N. E., Herold, M., Bertels, L., & Smets, B. (2020). Copernicus global land cover layers–collection 2, *Remote Sensing*, 12, 1044.

Brown, C. F., Brumby, S. P., Guzder-Williams, B., Birch, T., Hyde, S. B., Mazzariello, J., Czerwinski, W., Pasquarella, V.J., Haertel, R., Ilyushchenko, S. and Schwehr, K (2022). Dynamic World, Near real-time global 10 m land use land cover mapping. *Scientific Data*, *9*(1), 251.

Carrara, A. (1988). Drainage and divide networks derived from high-fidelity digital terrain models. In *Quantitative Analysis of Mineral and Energy Resources* (pp. 581-597). Dordrecht: Springer Netherlands.

Chen, Y., He, Y., Zhang, L., Chen, Y., Pu, H., Chen, B., & Gao, L. (2021). Prediction of InSAR deformation time-series using a long short-term memory neural network. *International Journal of Remote Sensing*, 42(18), 6919-6942.

Chleborad, A. F., Baum, R. L., & Godt, J. W. (2006). Rainfall thresholds for forecasting landslides in the Seattle, Washington, area: Exceedance and probability. US Geological Survey Open-File Report, 1064, 31.

Cortes, C., & Vapnik, V. (1995). Support-vector networks. *Machine Learning*, *20*, 273-297.

Cox, D. R. (1958). The regression analysis of binary sequences. *Journal of the Royal Statistical Society Series B: Statistical Methodology*, *20*(2), 215-232.

Das, S., Sharma, P., Pain, A., Kanungo, D. P., & Sarkar, S. (2023). Deep learning based landslide detection using open-source resources: Opportunities and challenges. *Earth Science Informatics*, 16(4), 4035-4052.

D'Ambrosio, D., Di Gregorio, S., & Iovine, G. (2003). Simulating debris flows through a hexagonal cellular automata model: sciddica s 3–hex. *Natural Hazards and Earth System Sciences*, 3(6), 545-559.

Deijns, A. A., Dewitte, O., Thiery, W., d'Oreye, N., Malet, J. P., & Kervyn, F. (2022). Timing landslide and flash flood events from SAR satellite: a regionally applicable methodology illustrated in African cloud-covered tropical environments. *Natural Hazards and Earth System Sciences*, *22*(11), 3679-3700.

Duc, D. M. (2013). Rainfall-triggered large landslides on 15 December 2005 in Van Canh district, Binh Dinh province, Vietnam. *Landslides*, *10*(2), 219-230.

Duc, D. M., Yen, H. H., & Minh, V. C. (2022, November). The Main Characteristics of the Large Landslide in the Northern Mountainous Region of Vietnam. In ISRM International Symposium-Asian Rock Mechanics Symposium (pp. ISRM-ARMS12). ISRM.

Endo, T. (1970). Probable distribution of the amount of rainfall causing landslides.

Fang, Z., Wang, Y., Peng, L., & Hong, H. (2020). Integration of convolutional neural network and conventional machine learning classifiers for landslide susceptibility mapping. *Computers & Geosciences*, 139, 104470.

Fang, Z., Tanyas, H., Gorum, T., Dahal, A., Wang, Y., & Lombardo, L. (2023). Speech-recognition in landslide predictive modelling: A case for a next generation early warning system. *Environmental Modelling & Software*, *170*, 105833.

Funk, C., Peterson, P., Landsfeld, M., Pedreros, D., Verdin, J., Shukla, S., Husak, G., Rowland, J., Harrison, L., Hoell, A. & Michaelsen, J. (2015). The climate hazards infrared precipitation with stations—a new environmental record for monitoring extremes. *Scientific data*, *2*(1), 1-21.

Frattini, P., Crosta, G., Carrara, A., & Agliardi, F. (2008). Assessment of rockfall susceptibility by integrating statistical and physically-based approaches. *Geomorphology*, *94*(3-4), 419-437.

Gariano, S. L., & Guzzetti, F. (2016). Landslides in a changing climate. *Earth-Science Reviews*, *162*, 227-252.

Gian, Q. A., Tran, D. T., Nguyen, D. C., Nhu, V. H., & Tien Bui, D. (2017). Design and implementation of site-specific rainfall-induced landslide early warning and monitoring system: a case study at Nam Dan landslide (Vietnam). *Geomatics, Natural Hazards and Risk*, *8*(2), 1978-1996.

Gupta, V., Jain, M. K., Singh, P. K., & Singh, V. (2020). An assessment of global satellite-based precipitation datasets in capturing precipitation extremes: A comparison with observed precipitation dataset in India. *International Journal of Climatology*, *40*(8), 3667-3688.

Guzzetti, F., Carrara, A., Cardinali, M., & Reichenbach, P. (1999). Landslide hazard evaluation: a review of current techniques and their application in a multi-scale study, Central Italy. *Geomorphology*, *31*(1-4), 181-216.

Guzzetti, F., Mondini, A. C., Cardinali, M., Fiorucci, F., Santangelo, M., & Chang, K. T. (2012). Landslide inventory maps: New tools for an old problem. *Earth-Science Reviews*, *112*(1-2), 42-66.

Han, K., Xiao, A., Wu, E., Guo, J., Xu, C., & Wang, Y. (2021). Transformer in transformer. *Advances in Neural Information Processing Systems*, 34, 15908-15919.

Hao, L., Van Westen, C., KS, S., Martha, T. R., Jaiswal, P., & McAdoo, B. (2020). Constructing a complete landslide inventory dataset for the 2018 monsoon disaster in Kerala, India, for land use change analysis. *Earth System Science Data Discussions*, *2020*, 1-32.

Hartmann, J., & Moosdorf, N. (2012). The new global lithological map database GLiM: A representation of rock properties at the Earth surface. *Geochemistry, Geophysics, Geosystems*, *13*(12).

Huffman, G. J., Bolvin, D. T., Braithwaite, D., Hsu, K., Joyce, R., Xie, P., & Yoo, S. H. (2015). NASA global precipitation measurement (GPM) integrated multi-satellite retrievals for GPM (IMERG). *Algorithm theoretical basis document (ATBD) version*, *4*(26), 30.

Hung, L. Q., Van, N. T. H., Son, P. V., Ninh, N. H., Tam, N., & Huyen, N. T. (2017). Landslide inventory mapping in the fourteen northern provinces of Vietnam: achievements and difficulties. In Advancing Culture of Living with Landslides: Volume 1 ISDR-ICL Sendai Partnerships 2015-2025 (pp. 501-510). Springer International Publishing.

Ioffe, S., & Szegedy, C. (2015, June). Batch normalization: Accelerating deep network training by reducing internal covariate shift. In *International conference on machine learning* (pp. 448-456). Pmlr.

Intergovernmental Panel on Climate Change. Sixth Assessment Report, Climate Change (IPCC) 2022. Impacts, Adaptation and Vulnerability. Full Report, Final draft (Intergovernmental Panel on Climate Change, Geneva, 2021). https://www.ipcc.ch/report/ar6/wg2/.

Jamieson, K., & Talwalkar, A. (2016, May). Non-stochastic best arm identification and hyperparameter optimization. In *Artificial Intelligence and Statistics* (pp. 240-248). PMLR.

Kawabata, D., & Bandibas, J. (2009). Landslide susceptibility mapping using geological data, a DEM from ASTER images and an Artificial Neural Network (ANN). *Geomorphology*, *113*(1-2), 97-109.

Kingma, D. P., & Ba, J. (2014). Adam: A method for stochastic optimization. *arXiv preprint arXiv:1412.6980*.

Kouli, M., Loupasakis, C., Soupios, P., & Vallianatos, F. (2010). Landslide hazard zonation in high risk areas of Rethymno Prefecture, Crete Island, Greece. *Natural hazards*, *52*, 599-621.

LaValle, S. (1998). Rapidly-exploring random trees: A new tool for path planning. *Research Report 9811*.

Lee, S., Ryu, J. H., Won, J. S., & Park, H. J. (2004). Determination and application of the weights for landslide susceptibility mapping using an artificial neural network. *Engineering Geology*, *71*(3-4), 289-302.

Lepvrier, C., Faure, M., Van, V. N., Van Vu, T., Lin, W., Trong, T. T., & Hoa, P. T. (2011). North-directed Triassic nappes in Northeastern Vietnam (East Bac Bo). *Journal of Asian Earth Sciences*, 41(1), 56-68.

Le Minh, N., Truyen, P. T., Van Phong, T., Jaafari, A., Amiri, M., Van Duong, N., Van Bien, N., Duc, D. M., Prakash, I. & Pham, B. T. (2023). Ensemble models based on radial basis function network for landslide susceptibility mapping. *Environmental Science and Pollution Research*, 1-19.

Li, L., Jamieson, K., DeSalvo, G., Rostamizadeh, A., & Talwalkar, A. (2017). Hyperband: A novel bandit-based approach to hyperparameter optimization. *Journal of Machine Learning Research*, *18*(1), 6765-6816.

Loche, M., Alvioli, M., Marchesini, I., Bakka, H., & Lombardo, L. (2022). Landslide susceptibility maps of Italy: Lesson learnt from dealing with multiple landslide types and the uneven spatial distribution of the national inventory. *Earth-Science Reviews*, 104125.

Lu, P., Qin, Y., Li, Z., Mondini, A. C., & Casagli, N. (2019). Landslide mapping from multi-sensor data through improved change detection-based Markov random field. *Remote Sensing of Environment*, *231*, 111235.

Ma, Z., Mei, G., Prezioso, E., Zhang, Z., & Xu, N. (2021). A deep learning approach using graph convolutional networks for slope deformation prediction based on time-series displacement data. *Neural Computing and Applications*, 33(21), 14441-14457.

Mayoraz, F., & Vulliet, L. (2002). Neural networks for slope movement prediction. *International Journal of Geomechanics*, 2(2), 153-173.

Mondini, A. C., Guzzetti, F., & Melillo, M. (2023). Deep learning forecast of rainfall-induced shallow landslides. *Nature communications*, *14*(1), 2466.

Moreno, M., Lombardo, L., Crespi, A., Zellner, P. J., Mair, V., Pittore, M., van Westen, C.. & Steger, S. (2024). Space-time data-driven modeling of precipitation-induced shallow landslides in South Tyrol, Italy. *Science of the Total Environment*, 912, 169166.

Nava, L., Carraro, E., Reyes-Carmona, C., Puliero, S., Bhuyan, K., Rosi, A., Monserrat, O., Floris, M., Meena, S. R., Galve, J. P., & Catani, F. (2023). Landslide displacement forecasting using deep learning and monitoring data across selected sites. *Landslides*, 20(10), 2111-2129.

Novellino, A., Pennington, C., Leeming, K., Taylor, S., Alvarez, I. G., McAllister, E., Arnhardt, C. & Winson, A. (2024). Mapping landslides from space: A review. *Landslides*, 1-12.

Nguyen, L. C., Tien, P. V., & Do, T. N. (2020). Deep-seated rainfall-induced landslides on a new expressway: a case study in Vietnam. *Landslides*, 17(2), 395-407.

Nguyen, D. D., Van Le, H., & Pham, B. T. (2023). Landslide susceptibility modeling and mapping at Dien Bien province, Vietnam using Bagging based MLP neural network. In *IOP Conference Series: Materials Science and Engineering* (Vol. 1289, No. 1, p. 012020). IOP Publishing.

Nhu, H. V., Van Duong, B., & Vu, H. D. (2019). 3D slope stability modeling for landslide early warning design at Halong city area. *Journal of Mining and Earth Sciences*, *60*(6), 31-41.

Oh, H. J., & Pradhan, B. (2011). Application of a neuro-fuzzy model to landslide-susceptibility mapping for shallow landslides in a tropical hilly area. *Computers & geosciences*, *37*(9), 1264-1276.

O'Malley, T., Bursztein, E., Long, J., Chollet, F., Jin, H., Invernizzi, L., et al. (2019). Keras Tuner.

Park, J.Y., Lee, S.R., Lee, D.H., Kim, Y.T. and Lee, J.S., 2019. A regional-scale landslide early warning methodology applying statistical and physically based approaches in sequence. *Engineering Geology*, *260*, p.105193.

Pareek, N., Sharma, M. L., & Arora, M. K. (2010). Impact of seismic factors on landslide susceptibility zonation: a case study in part of Indian Himalayas. *Landslides*, *7*, 191-201.

Pecoraro, G., Calvello, M., & Piciullo, L. (2019). Monitoring strategies for local landslide early warning systems. *Landslides*, *16*, 213-231.

Pham, N. T. T., Nong, D., Sathyan, A. R., & Garschagen, M. (2020). Vulnerability assessment of households to flash floods and landslides in the poor upland regions of Vietnam. *Climate Risk Management*, *28*, 100215.

Pham, N. T. T., Nong, D., & Garschagen, M. (2021). Natural hazard's effect and farmers' perception: Perspectives from flash floods and landslides in remotely mountainous regions of Vietnam. *Science of the Total Environment*, 759, 142656.

Poggio, L., De Sousa, L. M., Batjes, N. H., Heuvelink, G., Kempen, B., Ribeiro, E., & Rossiter, D. (2021). SoilGrids 2.0: producing soil information for the globe with quantified spatial uncertainty. *Soil*, 7(1), 217-240.

Rana, K., Ozturk, U., & Malik, N. (2021). Landslide geometry reveals its trigger. *Geophysical Research Letters*, 48(4), e2020GL090848.

Rana, K., Malik, N., & Ozturk, U. (2022). Landsifier v1. 0: a Python library to estimate likely triggers of mapped landslides. *Natural Hazards and Earth System Sciences*, 22(11), 3751-3764.

Rana, K., Bhuyan, K., Ferrer, J. V., Cotton, F., Ozturk, U., Catani, F., & Malik, N. (2023). Landslide topology uncovers failure movements. arXiv preprint arXiv:2310.09631.

Reichenbach, P., Busca, C., Mondini, A. C., & Rossi, M. (2014). The influence of land use change on landslide susceptibility zonation: the Briga catchment test site (Messina, Italy). Environmental management, 54, 1372-1384.

Reichenbach, P., Rossi, M., Malamud, B. D., Mihir, M., & Guzzetti, F. (2018). A review of statistically-based landslide susceptibility models. *Earth-science reviews*, *180*, 60-91.

Ruder, S. (2016). An overview of gradient descent optimization algorithms. *arXiv preprint arXiv:1609.04747*.

Saito, H., Nakayama, D., & Matsuyama, H. (2010). Relationship between the initiation of a shallow landslide and rainfall intensity—duration thresholds in Japan. *Geomorphology*, 118(1-2), 167-175.

Samia, J., Temme, A., Bregt, A., Wallinga, J., Guzzetti, F., Ardizzone, F., & Rossi, M. (2017). Do landslides follow landslides? Insights in path dependency from a multi-temporal landslide inventory. *Landslides*, 14(2), 547-558.

Segoni, S., Battistini, A., Rossi, G., Rosi, A., Lagomarsino, D., Catani, F., Moretti, S. & Casagli, N. (2015). An operational landslide early warning system at regional scale based on space–time-variable rainfall thresholds. *Natural Hazards and Earth System Sciences*, 15(4), 853-861.

Segoni, S., Piciullo, L., & Gariano, S. L. (2018). A review of the recent literature on rainfall thresholds for landslide occurrence. *Landslides*, 15(8), 1483-1501.

Snoek, J., Larochelle, H., & Adams, R. P. (2012). Practical bayesian optimization of machine learning algorithms. *Advances in neural information processing systems*, 25.

Srivastava, N., Hinton, G., Krizhevsky, A., Sutskever, I., & Salakhutdinov, R. (2014). Dropout: a simple way to prevent neural networks from overfitting. *The Journal of Machine Learning Research*, *15*(1), 1929-1958.

Stanley, T. A., Kirschbaum, D. B., Sobieszczyk, S., Jasinski, M. F., Borak, J. S., & Slaughter, S. L. (2020). Building a landslide hazard indicator with machine learning and land surface models. *Environmental Modelling & Software*, *129*, 104692.

Stanley, T. A., Kirschbaum, D. B., Benz, G., Emberson, R. A., Amatya, P. M., Medwedeff, W., & Clark, M. K. (2021). Data-driven landslide nowcasting at the global scale. *Frontiers in Earth Science*, 9, 640043.

Stefanini, M. C. (2004). Spatio-temporal analysis of a complex landslide in the Northern Apennines (Italy) by means of dendrochronology. *Geomorphology*, *63*(3-4), 191-202.

Steger, S., Brenning, A., Bell, R., & Glade, T. (2016). The propagation of inventory-based positional errors into statistical landslide susceptibility models. *Natural Hazards and Earth System Sciences*, 16(12), 2729-2745.

Steger, S., Moreno, M., Crespi, A., Zellner, P. J., Gariano, S. L., Brunetti, M. T., Melillo, M., Peruccacci., S., Marra, F., Kohrs, R., Goetz, J., Mair, V. & Pittore, M. (2022). Deciphering seasonal effects of triggering and preparatory precipitation for improved shallow landslide prediction using generalized additive mixed models. *Natural Hazards and Earth System Sciences Discussions*, *2022*, 1-38.

Styron, R., & Pagani, M. (2020). The GEM global active faults database. *Earthquake Spectra*, *36*, 160-180

Tanyaş, H., & Luigi, L. (2020). Completeness index for earthquake-induced landslide inventories. *Engineering geology*, 264, 105331.

Thinh, P. H., Tuan, P. Q., & Minh, P. N. (2016, March). Prevention and remediation of rockslide at left portal of north tunnel of Da Nang–Qu ang Ngai expressway in Quang Nam, Vietnam. In IOP Conference Series: Earth and Environmental Science (Vol. 33, No. 1, p. 012045). IOP Publishing.

Tien Bui, D., Tuan, T. A., Hoang, N. D., Thanh, N. Q., Nguyen, D. B., Van Liem, N., & Pradhan, B. (2017). Spatial prediction of rainfall-induced landslides for the Lao Cai area (Vietnam) using a hybrid intelligent approach of least squares support vector machines inference model and artificial bee colony optimization. *Landslides*, *14*, 447-458.

Titti, G., van Westen, C., Borgatti, L., Pasuto, A., & Lombardo, L. (2021). When enough is really enough? On the minimum number of landslides to build reliable susceptibility models. *Geosciences*, 11(11), 469.

Vaswani, A., Shazeer, N., Parmar, N., Uszkoreit, J., Jones, L., Gomez, A. N., Kaiser, L. & Polosukhin, I. (2017). Attention is all you need. *Advances in neural information processing systems*, 30.

Van Tien, P., Luong, L. H., Duc, D. M., Trinh, P. T., Quynh, D. T., Lan, N. C., Thuy, D. T., Ngyuen, Q. P., Cuong, T. Q., Dang, K. & Loi, D. H. (2021). Rainfall-induced catastrophic landslide in Quang Tri Province: the deadliest single landslide event in Vietnam in 2020. *Landslides.*

Wang, Y., Fang, Z., & Hong, H. (2019). Comparison of convolutional neural networks for landslide susceptibility mapping in Yanshan County, China. Science of the total environment, 666, 975-993.

Yadav, R., Huser, R., Opitz, T., & Lombardo, L. (2023). Joint modelling of landslide counts and sizes using spatial marked point processes with sub-asymptotic mark distributions. *Journal of the Royal Statistical Society Series C: Applied Statistics*, *72*(5), 1139-1161.

Yamazaki, D., Ikeshima, D., Neal, J. C., O'Loughlin, F., Sampson, C. C., Kanae, S., & Bates, P. D. (2017). MERIT DEM: A new high-accuracy global digital elevation model and its merit to global hydrodynamic modeling. In *AGU Fall Meeting Abstracts* (Vol. 2017, pp. H12C-04).

Yang, Z., & Xie, M. (2000). Process monitoring of exponentially distributed characteristics through an optimal normalizing transformation. *Journal of Applied Statistics*, *27*(8), 1051-1063.

Youden, W. J. (1950). Index for rating diagnostic tests. *Cancer*, *3*(1), 32-35.

Zeng, H., Zhu, Q., Ding, Y., Hu, H., Chen, L., Xie, X., Chen, M., & Yao, Y. (2022). Graph neural networks with constraints of environmental consistency for landslide susceptibility evaluation. *International Journal of Geographical Information Science*, 36(11), 2270-2295.

Zêzere, J. L., Vaz, T., Pereira, S., Oliveira, S. C., Marques, R., & Garcia, R. A. (2015). Rainfall thresholds for landslide activity in Portugal: a state of the art. *Environmental Earth Sciences*, 73, 2917-2936.

Zêzere, J. L., Pereira, S., Melo, R., Oliveira, S. C., & Garcia, R. A. (2017). Mapping landslide susceptibility using data-driven methods. *Science of the Total Environment*, 589, 250-267.

Zhang, W., Zhang, Y., Gu, X., Wu, C., & Han, L. (2022). Application of LSTM and Prophet Algorithm in Slope Displacement Prediction. Application of Soft Computing, Machine Learning, Deep Learning and Optimizations in Geoengineering and Geoscience, 73-92.